



Viscoelastic flow analysis using the software OpenFOAM and differential constitutive equations

J.L. Favero^a, A.R. Secchi^b, N.S.M. Cardozo^{a,*}, H. Jasak^c

^a DEQUI/UFRGS - Departamento de Engenharia Química, Universidade Federal do Rio Grande do Sul, Porto Alegre, RS, Brazil

^b PEQ/COPPE - Universidade Federal do Rio de Janeiro, CT, Rio de Janeiro, RJ, Brazil

^c FSB/Wikki - Faculty of Mechanical Engineering and Naval Architecture, University of Zagreb, Croatia and Wikki Ltd., London, United Kingdom

ARTICLE INFO

Article history:

Received 3 July 2010

Received in revised form 25 August 2010

Accepted 29 August 2010

Keywords:

Viscoelastic flow

Planar contraction

Fluid mechanics

ViscoelasticFluidFoam

OpenFOAM

ABSTRACT

Viscoelastic fluids are of great importance in many industrial sectors, such as in food and synthetic polymers industries. The rheological response of viscoelastic fluids is quite complex, including combination of viscous and elastic effects and non-linear phenomena. This work presents a numerical methodology based on the split-stress tensor approach and the concept of equilibrium stress tensor to treat high Weissenberg number problems using any differential constitutive equations. The proposed methodology was implemented in a new computational fluid dynamics (CFD) tool and consists of a viscoelastic fluid module included in the OpenFOAM, a flexible open source CFD package. Oldroyd-B/UCM, Giesekus, Phan-Thien–Tanner (PTT), Finitely Extensible Nonlinear Elastic (FENE-P and FENE-CR), and Pom–Pom based constitutive equations were implemented, in single and multimode forms. The proposed methodology was evaluated by comparing its predictions with experimental and numerical data from the literature for the analysis of a planar 4:1 contraction flow, showing to be stable and efficient.

© 2010 Elsevier B.V. All rights reserved.

1. Introduction

Processing operations involving viscoelastic melts, solutions, or suspensions are usually the key step in the definition of the characteristics and quality of the finished products in polymer and food industries. Therefore, understanding and modeling viscoelastic flows is of fundamental importance in these industrial sectors. The rheological response of viscoelastic fluids is quite complex, including combination of non-linear viscous and elastic effects, such as strain rate dependent viscosity, presence of normal stress differences in shear flows, relaxation phenomena, and memory effects, including die swell [1,2].

Numerous studies on the numerical analysis of viscoelastic flows using one or more non-linear differential models can be found in literature. A common difficulty in all these works, regardless of the discretization method (finite element, finite differences, or finite volume), iterative solution method, or constitutive equations used, is the so-called ‘High Weissenberg Number Problem’ (HWNP). The HWNP consists in the difficulty of achieving convergence at high Weissenberg (We) or Deborah (De) numbers, where the dimensionless numbers We and De are ratios between a characteristic relaxation time of the polymer and a characteristic flow

time. The higher the Weissenberg (or Deborah) number, the more pronounced the elastic effect. In the attempt of solving the HWNP or minimizing its effects, many strategies have been proposed, including special interpolations schemes [3,4] and specific numerical methodologies coupling momentum and constitutive viscoelastic equations [5–8].

Another relevant aspect regarding the analysis of viscoelastic flows is the development of software specifically designed for this purpose. Despite the extensive literature on viscoelastic behavior modeling and viscoelastic flow simulation, most of commercial packages intended to be applied to the analysis of polymeric flows and polymer processing operations, such as extrusion and injection molding, are actually limited to the description of purely viscous non-Newtonian phenomena. Development and use of software with viscoelastic flow analysis capability is still carried out almost exclusively in academic environments, for specific applications.

According to this scenario the insertion of a viscoelastic fluid flow solver in a widely recognized CFD (*computational fluid dynamics*) package is a relevant matter, since it would bring to viscoelastic fluid flow analysis field the main features of CFD packages, which include the possibility of analyzing complex geometries using unstructured and non-orthogonal meshes, moving meshes, large variety of interpolation schemes and solvers for the linear discretized system, data processing parallelization among others benefits.

Being a well-tested and widely used free open source CFD package, with the intrinsic advantages of being written in the C++ object-oriented language, in this context the OpenFOAM (*Open*

* Corresponding author at: Rua Luis Englert, s/n., CEP 90040-040, Porto Alegre, RS, Brazil. Tel.: +55 51 3308 4075.

E-mail addresses: jovani.favero@gmail.com (J.L. Favero), arge@peq.coppe.ufrj.br (A.R. Secchi), nilo@enq.ufrgs.br (N.S.M. Cardozo), h.jasak@wikki.co.uk (H. Jasak).

Source Field Operation and Manipulation) package [9,10] appears as a promising tool for this kind of development. The flexibility to deal with unstructured and moving meshes and to implement complex mathematical models are some of its attractive features.

Therefore, the goal of this work was to create a general purpose viscoelastic fluid flow solver to be used in OpenFOAM CFD package. For this, a numerical methodology based on the split-stress tensor approach [6–8,11] and on the concept of equilibrium stress tensor was developed to treat the HWNP and deal with any differential constitutive equations. The so-called viscoelasticFluidFoam solver was evaluated by comparing its predictions with experimental and numerical data from the literature for the analysis of a planar 4:1 contraction flow.

2. Methodology

In this section the mathematical formulation and the main aspects related to the viscoelasticFluidFoam solver are presented. The case study used to evaluate the solver is also presented.

2.1. Mathematical model

The governing equations for isothermal incompressible flows of viscoelastic fluids are the mass conservation (continuity):

$$\nabla \cdot (\mathbf{u}) = 0 \quad (1)$$

and momentum conservation:

$$\frac{\partial(\rho \mathbf{u})}{\partial t} + \nabla \cdot (\rho \mathbf{u} \mathbf{u}) = -\nabla p + \nabla \cdot \boldsymbol{\tau} \quad (2)$$

together with a constitutive equation to describe the relation between the stress and deformation rate for the fluid of interest. In the above equations ρ is the density of the fluid, \mathbf{u} the velocity vector, p the pressure, and $\boldsymbol{\tau}$ the stress tensor.

The stress tensor can be divided into a Newtonian solvent contribution $\boldsymbol{\tau}_S$ and an elastic polymeric contribution (or extra elastic stress tensor) $\boldsymbol{\tau}_P$:

$$\boldsymbol{\tau} = \boldsymbol{\tau}_S + \boldsymbol{\tau}_P \quad (3)$$

with $\boldsymbol{\tau}_S$ defined by:

$$\boldsymbol{\tau}_S = 2\eta_S \mathbf{D} \quad (4)$$

where η_S is the solvent viscosity and \mathbf{D} is the deformation rate tensor given by:

$$\mathbf{D} = \frac{1}{2}(\nabla \mathbf{u} + [\nabla \mathbf{u}]^T) \quad (5)$$

The $\boldsymbol{\tau}_P$ is a symmetric tensor obtained as the sum of the contributions of the individual relaxation modes:

$$\boldsymbol{\tau}_P = \sum_{K=1}^n \boldsymbol{\tau}_{P_K} \quad (6)$$

with the expression for $\boldsymbol{\tau}_{P_K}$ depending on the viscoelastic constitutive equation.

The differential constitutive equations used in this work are presented in Table 1. Since all these equations are well known and extensively used in the literature, the expressions for the upper convected ($\overset{\nabla}{\boldsymbol{\tau}}_{P_K}$), lower convected ($\overset{\Delta}{\boldsymbol{S}}_{P_K}$) and Gordon–Schowalter ($\overset{\square}{\boldsymbol{\tau}}_{P_K}$) derivatives, and the meaning of the parameters which appear in the models of Table 1 are not shown here. The expressions for the mentioned derivatives can be found in classic rheology books [1,2], while for detailed information about these models and their parameters the reader is suggested to refer to [12–22].

2.2. Pressure–velocity and momentum–stress coupling and tensorial viscosity

Velocity–pressure coupling was accomplished by segregated methods, in which the continuity equation is used to formulate an equation for the pressure, using a semi-discretized form of Eq. (2)[23]. The resulting equation set is solved by a decoupled approach, using iterative algorithms with under-relaxation, such as SIMPLE [24].

Regarding momentum–stress coupling and numerical stabilization in the solution of the momentum equation, the strategy employed consists of decomposing the viscoelastic stress into an implicit component aligned with \mathbf{D} , defined on the basis of a tensorial viscosity $\boldsymbol{\eta}_T$, and an explicit correction:

$$\nabla \cdot \boldsymbol{\tau} \approx \nabla \cdot (\boldsymbol{\eta}_T \cdot \nabla \mathbf{u}) + \nabla \cdot \boldsymbol{\tau}_{\text{corr}} \quad (7)$$

Additionally, the stress transport models were written in the following generic form:

$$\frac{\partial}{\partial t} \boldsymbol{\tau} + \nabla \cdot (\mathbf{u} \boldsymbol{\tau}) = \frac{\boldsymbol{\tau}^* - \boldsymbol{\tau}}{\lambda} \quad (8)$$

This equation describes transport of $\boldsymbol{\tau}$ in space by the velocity field, with simultaneous relaxation towards the equilibrium value $\boldsymbol{\tau}^*$, where $\boldsymbol{\tau}^*$ is the stress state achieved in the absence of transport effects and λ is the relaxation time scale. It is possible to achieve this form irrespective of the specific model used. For multi-mode versions of the stress models, each mode will present its own equilibrium stress, which can be combined in the usual manner.

From Eq. (8), one can clearly see that $\boldsymbol{\tau}^*$ must be related to the local value of \mathbf{D} , specifically because it excludes the effects of relaxation and transport. Furthermore, the magnitude of $\boldsymbol{\eta}_T$, that is related with \mathbf{D} and $\boldsymbol{\tau}^*$, will be considerably higher than the Newtonian viscosity (Eq. (4)), whose effective contribution is generally not significant for realistic non-linear flows of polymeric melts. This higher magnitude of $\boldsymbol{\eta}_T$ represents a key aspect in the methodology used in this work, since the stability in the numerical solution of the momentum equation is strongly dependent on the magnitude of the implicit Laplacian-like term.

A consistent and model-independent expression for $\boldsymbol{\eta}_T$ may be obtained based on the definition:

$$\boldsymbol{\tau}^* = \boldsymbol{\eta}_T \cdot \mathbf{D} \quad (9)$$

from which:

$$\boldsymbol{\eta}_T = \boldsymbol{\tau}^* \cdot \mathbf{D}^{-1} \quad (10)$$

For cases where $\det(\mathbf{D})=0$ (implying that a velocity gradient is a singular tensor), $\boldsymbol{\eta}_T = \mathbf{0}$ or $\boldsymbol{\eta}_T = \eta_P \mathbf{I}$ are adequate choices. For multi-mode versions of the stress models, components of $\boldsymbol{\eta}_T$ can be summed up in the same manner as constituent stress tensors.

In this formulation, the momentum equation was implemented in the following form:

$$\frac{\partial(\rho \mathbf{u})}{\partial t} + \nabla \cdot (\rho \mathbf{u} \mathbf{u}) - \nabla \cdot (\boldsymbol{\eta}_T \cdot \nabla \mathbf{u}) = -\nabla p + \nabla \cdot \boldsymbol{\tau}_{\text{corr}} \quad (11)$$

where the dominant Laplacian-like term, $\nabla \cdot (\boldsymbol{\eta}_T \cdot \nabla \mathbf{u})$ guarantees stability through implicit treatment, while the correction term $\nabla \cdot \boldsymbol{\tau}_{\text{corr}}$ is simply calculated as the difference between the divergence of the instantaneous stress $\boldsymbol{\tau}$ and the implicit counterpart, i.e., the term $\nabla \cdot (\boldsymbol{\eta}_T \cdot \nabla \mathbf{u})$. Note that $\nabla \cdot \boldsymbol{\tau}_{\text{corr}}$ also carries the relaxation component $(\boldsymbol{\tau} - \boldsymbol{\tau}^*)$, which tends to zero over the relaxation time-scale λ .

For segregated approaches, one can further simplify the tensorial Laplacian-like $\nabla \cdot (\boldsymbol{\eta}_T \cdot \nabla \mathbf{u})$, using a decomposition into a spherical component of $\boldsymbol{\eta}_T$, with the deviatoric part being absorbed into $\boldsymbol{\tau}_{\text{corr}}$.

Table 1
Constitutive differential equations [1,2,16].

Model name	Equation
Oldroyd-B/UCM	$\tau_{pK} + \lambda_K \overset{\nabla}{\tau}_{pK} = 2\eta_{pK} \mathbf{D}$
Giesekus	$\tau_{pK} + \lambda_K \overset{\nabla}{\tau}_{pK} + \alpha_K \frac{\lambda_K}{\eta_{pK}} (\tau_{pK} \cdot \tau_{pK}) = 2\eta_{pK} \mathbf{D}$
FENE-P	$\left(1 + \frac{(3)/(1-3/L_K^2) + \lambda_K/\eta_{pK} \text{tr}(\tau_{pK})}{L_K^2}\right) \tau_{pK} + \lambda_K \overset{\nabla}{\tau}_{pK} = 2 \frac{1}{(1-3/L_K^2)} \eta_{pK} \mathbf{D}$
FENE-CR	$\left(\frac{L_K^2 + (\lambda_K)/(\eta_{pK} \text{tr}(\tau_{pK}))}{(L_K^2 - 3)}\right) \tau_{pK} + \lambda_K \overset{\nabla}{\tau}_{pK} = 2 \left(\frac{L_K^2 + (\lambda_K)/(\eta_{pK} \text{tr}(\tau_{pK}))}{(L_K^2 - 3)}\right) \eta_{pK} \mathbf{D}$
LPIT	$\left(1 + \frac{\epsilon_K \lambda_K}{\eta_{pK}} \text{tr}(\tau_{pK})\right) \tau_{pK} + \lambda_K \overset{\square}{\tau}_{pK} = 2\eta_{pK} \mathbf{D}$
EPTT	$\exp\left(\frac{\epsilon_K \lambda_K}{\eta_{pK}} \text{tr}(\tau_{pK})\right) \tau_{pK} + \lambda_K \overset{\square}{\tau}_{pK} = 2\eta_{pK} \mathbf{D}$
DCPP	$\left[\left(1 - \frac{\xi_K}{2}\right) \overset{\nabla}{\mathbf{S}}_{pK} + \frac{\xi_K}{2} \overset{\Delta}{\mathbf{S}}_{pK}\right] + (1 - \xi_K)[2\mathbf{D} : \mathbf{S}_{pK}] \mathbf{S}_{pK} + \frac{1}{\lambda_{ObK} \Lambda_{pK}^2} \left[\mathbf{S}_{pK} - \frac{\delta}{3}\right] = 0$ $\frac{D(\Lambda_{pK})}{Dt} = \Lambda_{pK} [\mathbf{D} : \mathbf{S}_{pK}] - \frac{1}{\lambda_{SK}} [\Lambda_{pK} - 1], \quad \lambda_{SK} = \lambda_{ObK} \exp^{-\frac{2}{q}(\Lambda_{pK} - 1)}$ $\tau_{pK} = \frac{\eta_{pK}}{(1 - \xi_K) \lambda_{ObK}} (3 \Lambda_{pK}^2 \mathbf{S}_{pK} - \delta)$

2.3. Numerical algorithm

The procedure used to solve the problem of viscoelastic fluid flow can be summarized in the following four steps (the programming details are given in [Appendix A](#)):

1. For given initial fields of velocity \mathbf{u} , pressure p , and stress τ , the explicit calculations of the pressure gradient and the stress divergence are carried out, and, subsequently, the momentum equation is solved implicitly for each component of the velocity vector, computing a new velocity field estimate \mathbf{u}^* .
2. With the new velocity values \mathbf{u}^* , the new pressure field p^* is estimated and, subsequently, the correction of velocity is carried out, leading to a new velocity field \mathbf{u}^{**} which satisfies the continuity equation. In this step either SIMPLE [24] or PISO [25] algorithm can be used to obtain p^* and \mathbf{u}^{**} , with the more accurate PISO being the best option for transient flows.
3. With the corrected velocity field \mathbf{u}^{**} , the new estimate τ^* for the stress tensor field is calculated by solving the specified constitutive equation.
4. Steps 1, 2 and 3 may be repeated recursively within each time step in order to generate more accurate solutions in transient flows. For this, \mathbf{u} , p and τ are updated with \mathbf{u}^{**} , p^* and τ^* , respectively.

2.4. Test geometry and flow conditions

A planar abrupt contraction with contraction ratio H/h of 3.97:1 (upstream thickness of $2H=0.0254$ m and downstream thickness of $2h=0.0064$ m) was chosen as test geometry ([Fig. 1](#)), because of the availability of literature data for testing the developed code. Quinzani et al. [26] presented an extensive experimental study on this geometry using LDV (*Laser-Doppler Velocimetry*) and FIB

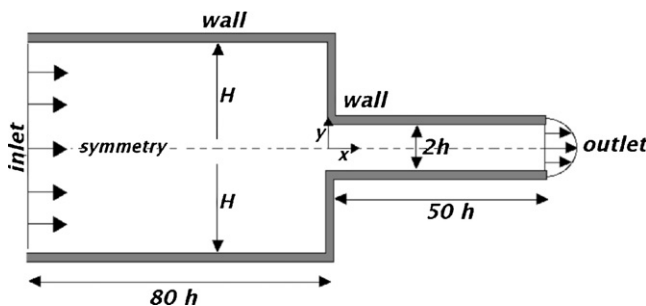


Fig. 1. Sketch of geometry and the boundary conditions.

(*Flow Induced Birefringence*) for stress measurements on a polymer solution of 5 wt.% of polyisobutylene (PIB) in tetradecane (C_{14}) ($\rho = 803.87 \text{ kg m}^{-3}$). Azaiez et al. [28] compared these experimental results with numerical predictions using the finite element method (FEM) and the Giesekus model.

A detailed study for the velocity and stress field was done to a single condition of flow, corresponding to Run 5 of Ref. [26]. The flow is characterized by two-dimensionless numbers, the Reynolds and Deborah numbers.

$$Re_0 = \frac{2\rho\langle u \rangle h}{\eta_0}, \quad De_0 = \frac{\lambda\langle \dot{\gamma} \rangle}{h} = \lambda\langle \dot{\gamma} \rangle \quad (12)$$

where $\langle u \rangle$ is the average velocity in the downstream channel, η_0 is the sum of the solvent and polymer contribution $\eta_0 = \eta_p + \eta_s$ and $\langle \dot{\gamma} \rangle$ is the characteristic shear rate, given by:

$$\langle \dot{\gamma} \rangle = \frac{\langle u \rangle}{h}, \quad \langle u \rangle = \frac{Q}{2Wh} \quad (13)$$

with W being the width of the channel and Q the volumetric flow rate. [Table 2](#) shows flow conditions used in Run 5 of Ref. [26].

In the analysis, the following boundary conditions were used for velocity: no-slip at the walls (*wall condition*), symmetry (*symmetry condition*) at the centerline, uniform profile at the entrance (*inlet condition*) with the prescribed velocity being given by the downstream average velocity divided by four, and a Neumann condition at the exit (*outlet condition*), setting the velocity derivative to zero in the flow direction. Boundary conditions for the momentum equation also include the value of pressure at the exit, which was set to zero. The stress tensor was set to zero at the inlet and zero gradient condition was used at the remaining boundaries.

Crank–Nicolson method was used for time derivatives, with zero initial condition being specified for all variables. The resulting linear discretized systems were solved by conjugated gradient method (CG), using PCG with AMG preconditioning for pressure and BiCGstab with a Incomplete Lower-Upper (ILU) preconditioning for velocity and stress [29–31]. The absolute tolerance for pressure was 1.0×10^{-7} and for velocity and stress was 1.0×10^{-6} .

Table 2
Flow conditions.

$Q [\text{cm}^3 \text{s}^{-1}]$	$\langle u \rangle [\text{cm s}^{-1}]$	$\langle \dot{\gamma} \rangle [\text{s}^{-1}]$	Re_0	De_0
252	15.5	48.4	0.56	1.45 ^a

^a Quinzani et al. [26] chose the UCM (“Upper Convected Maxwell”) model to fit the linear viscoelastic properties with a relaxation time of $\lambda = 0.06$ s, so their $De_0 = 2.90$ [32].

Table 3
Parameters of the constitutive equations used in this work.

Model	Non-linear parameter	λ [s]	η_p [Pa s]	η_s [Pa s]
Giesekus	$\alpha = 0.15$	0.03	1.422	0.002
LPTT	$\epsilon = 0.25, \xi = 0.0$	0.03	1.422	0.002
FENE-P	$L^2 = 6.0$	0.04	1.422	0.002

2.5. Parameters of the constitutive models

The Giesekus, LPTT, FENE-P and DCPD constitutive equations were used in the simulations. The parameters used for single-mode Giesekus, LPTT and FENE-P, showed in Table 3, are those of Ref. [28] which were obtained by fitting the model to the experimental data of Quinzani et al. [26]. For multimode Giesekus and DCPD models the parameters are presented in the corresponding result section.

3. Results and discussion

In the following sections the results corresponding to the different steps of the solver evaluation are presented. These steps include: (i) mesh convergence tests, analysis of performance of different interpolations schemes for the convective terms, and comparison of the predictions of the viscoelasticFluidFoam solver with numerical and experimental results from literature, using a single-mode Giesekus model; (ii) tests with multimode Giesekus; (iii) test for LPTT and FENE-P models; and (iv) tests with multimode DCPD.

3.1. Evaluation of the viscoelasticFluidFoam basic structure using the single-mode Giesekus constitutive model

3.1.1. Mesh convergence analysis

The characteristics of the three hexahedral meshes used for mesh convergence analysis are presented in Table 4 and the intermediate mesh (Mesh 2) is shown in Fig. 2. All meshes were designed with higher refinement near the walls and in the contraction, as shown in Fig. 2 for Mesh 2, because these two regions are known to present the largest gradient values for the variables under consideration.

The predicted velocity, shear stress and first normal stress difference profiles obtained with the three meshes are compared in

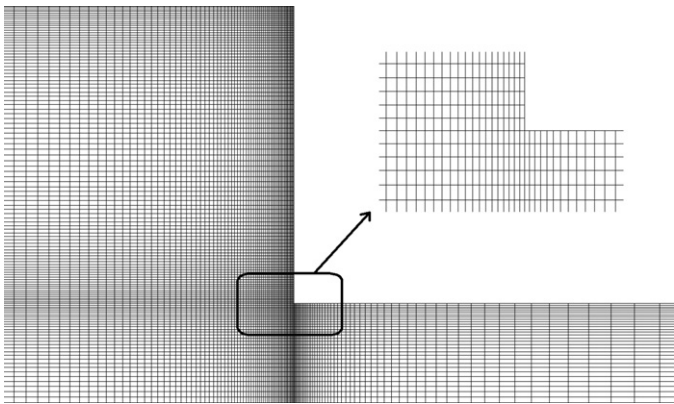


Fig. 2. Computational grid.

Figs. 3–7. In all these figures the greatest differences among the predictions with the three meshes are observed in the curves corresponding to the lines closest to the contraction corner (curve “a” of each figure). Additionally, it can be noticed that the differences are more significant for shear stress and normal stress difference than for velocity, especially when comparing the values obtained with meshes 1 and 3.

To provide a quantitative comparison among these results a percentage normalized error (PNE) was defined in the following way:

$$PNE = \max_{j=1}^N \left(\frac{|X_j^i - X_j^{ref}|}{\max(|X^{ref}|)} \right) \times 100 \tag{14}$$

where X_j^i is the value of the considered variable at a mesh point j of the line “a” (Figs. 3–5), N is the number of discretization points on the line “a”, i is the index used to indicate Mesh 1 or 2, and X^{ref} are the values obtained with Mesh 3 which is taken as reference. The values of PNE for velocity, shear stress and first normal stress in meshes 1 and 2 are shown in Table 5. For all variables, reduction of PNE was observed when comparing Mesh 2 to Mesh 1, indicating mesh convergence. Additionally, the fact that the values of PNE for Mesh 2 were all lower than 2.5% indicates that this mesh ensures

Table 4
Characteristics of the three meshes used for mesh convergence analysis.

Mesh	Upstream		Downstream		$\Delta x_{min}/h$	$\Delta y_{min}/h^a$	Numbers of control volumes
	N_x	N_y	N_x	N_y			
1	100	80	60	20	0.0098	0.026	9200
2	150	120	90	30	0.0065	0.017	20,700
3	200	160	120	40	0.0049	0.013	36,800

^a $\Delta x_{min}/h$ and $\Delta y_{min}/h$ correspond to measures of the mesh dimensions in the smallest volume control next to re-entrant corner normalized with the half-height of the downstream channel.

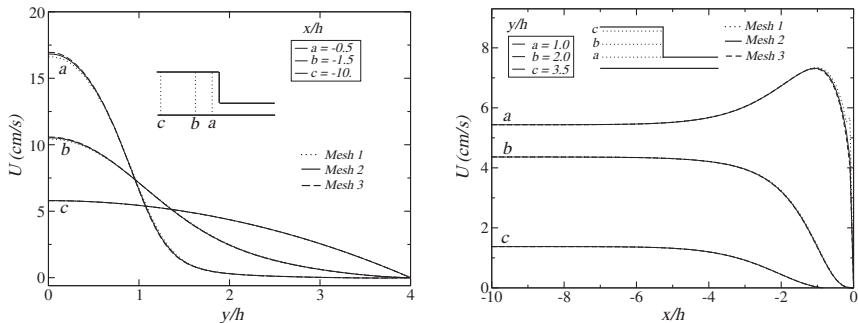


Fig. 3. Velocity profile U_x in the upstream section for meshes 1, 2 and 3 using the single-mode Giesekus model.

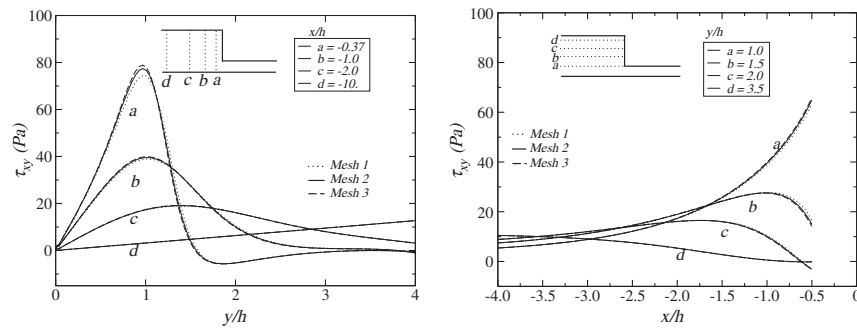


Fig. 4. Stress profile τ_{xy} in the upstream section for meshes 1, 2 and 3 using the single-mode Giesekus model.

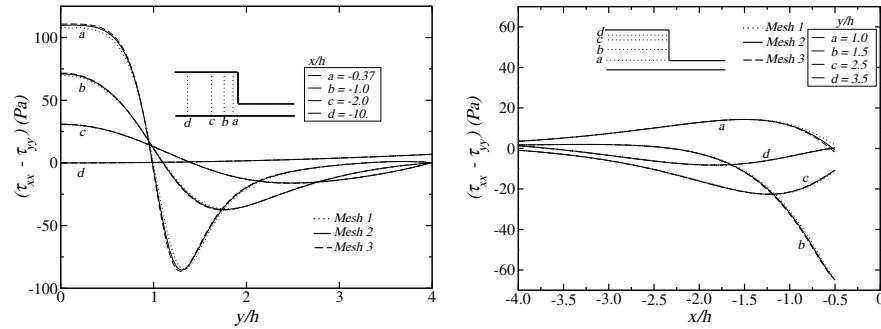


Fig. 5. First normal stress difference profile N_1 in the upstream section for meshes 1, 2 and 3 using the single-mode Giesekus model.

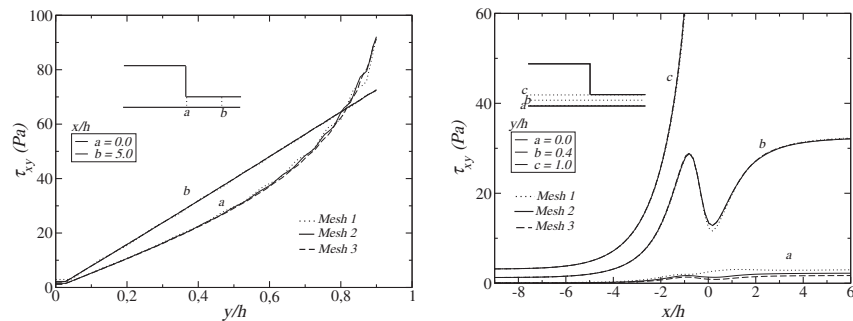


Fig. 6. Stress profile τ_{xy} in the downstream section for meshes 1, 2 and 3 using the single-mode Giesekus model.

the desired accuracy with lower computational cost than *Mesh 3*. So, *Mesh 2* was used in all tests discussed in the next sections.

3.1.2. Performance of the different interpolation schemes for the convective term

The selection of an adequate interpolation scheme for the convective terms is a critical issue in the analysis of fluid flows, since an

inappropriate choice may introduce instabilities and oscillations in the solution. In this work, four interpolation schemes were tested: first order *upwind* scheme, *MinMod* scheme, *Gamma* differencing, and *SFCD* (Self-Filtered Central Differencing) [33–35]. *MinMod* is a high-resolution scheme which combines the central differencing and second order *upwind* base schemes. *Gamma* differencing and *SFCD* are examples of NVD (*Normalized Variable Diagram*) schemes.

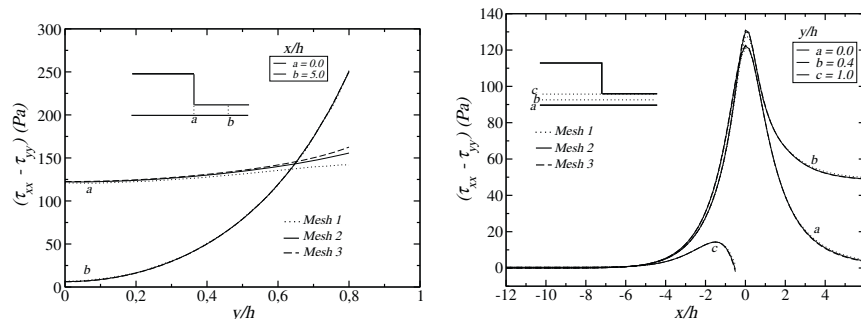


Fig. 7. First normal stress difference profile N_1 in the downstream section for meshes 1, 2 and 3 using the single-mode Giesekus model.

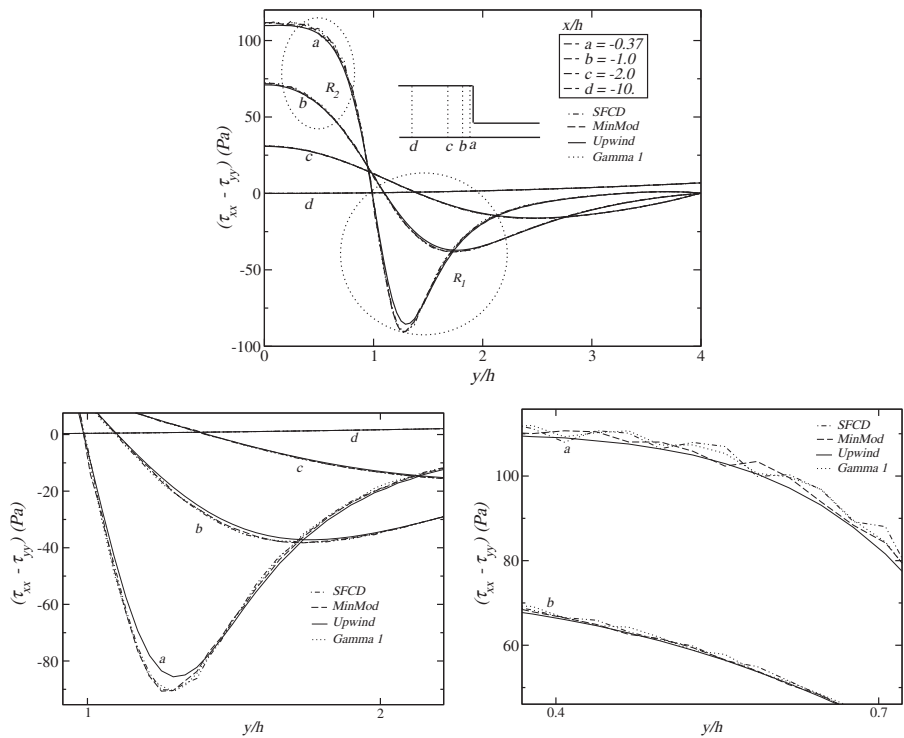


Fig. 8. First normal stress difference profiles in the upstream section using the single-mode Giesekus model: complete profiles for lines “a”, “b”, “c” and “d” (top), zoom of region R_1 (bottom left), and zoom of region R_2 (bottom right).

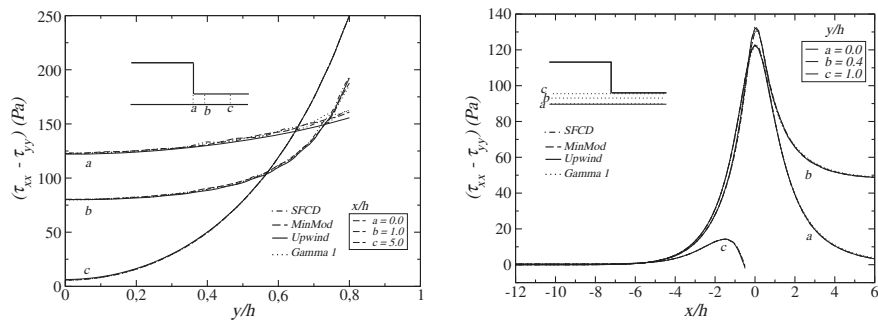


Fig. 9. First normal stress difference profiles (using the single-mode Giesekus model) on vertical lines in the downstream section (left) and on horizontal lines crossing the flow domain (right).

In all tests with the *Gamma* differencing scheme a value of $\gamma = 1$ was used, which corresponds to the least dissipative option [33].

Velocity profiles are not shown because practically no influence of the interpolation schemes on this variable was observed. Profiles of shear stress and first normal stress difference presented the same qualitative behavior in terms of influence of the interpolation schemes, with the most pronounced effect occurring for the first normal stress difference. Due to that only results of the latter variable are presented (Figs. 8 and 9).

Fig. 8 presents the profiles of first normal stress difference on four vertical lines located in the upstream section. Observation of the complete profiles (Fig. 8, top) reveals that the greatest differ-

ences among the schemes occur nearby the contraction, where the highest values of elongation rate and, consequently, of stress are found. A zoom of this region (Fig. 8, bottom left) is used to facilitate the comparison of the predictions of the four interpolation schemes, showing that *MinMod*, *SFCD* and *Gamma 1* schemes lead to quite similar results and that the *upwind* scheme presented significant deviations with relation to the other three schemes. On the other hand, the upwind scheme was the only scheme to produce oscillation free solutions at regions of high elongation rate, while *SFCD* was the scheme that introduced the highest oscillations in these regions (Fig. 8, bottom right).

Fig. 9 shows first normal stress profiles on vertical lines located in the downstream section (Fig. 9, left) and on horizontal lines crossing the entire flow domain (Fig. 9, right). As it can be seen from the first stress difference on the vertical lines “a” and “b” of Fig. 9 (left), also in the downstream section, the highest differences among the predictions of the four interpolation schemes take place nearby the contraction. Additionally, far from the contraction the four schemes led to practically identical results (Fig. 9, right), despite the higher shear rate levels in the downstream section. These results also indicate that the influence of the elongation

Table 5
Percentage normalized error of the meshes 1 and 2 with relation to the mesh 3 for the curve “a” in Figs. 3–5.

Mesh	PNE		
	U	τ_{xy}	N_1
1	2.034	3.068	6.329
2	0.729	1.054	2.118

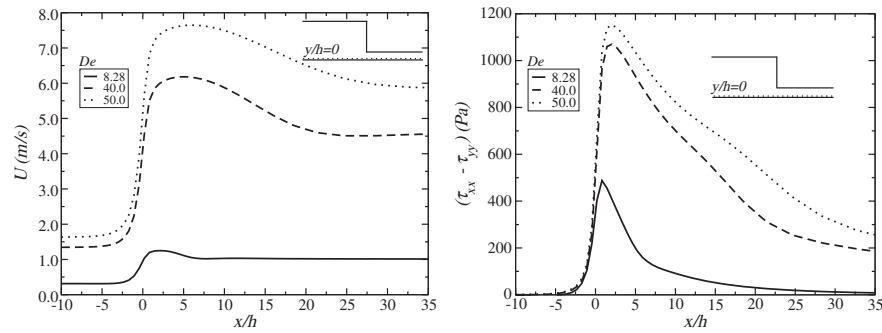


Fig. 10. Effects of Deborah number on the velocity field and on the first normal stress difference profile along the centerline using the single-mode Giesekus model.

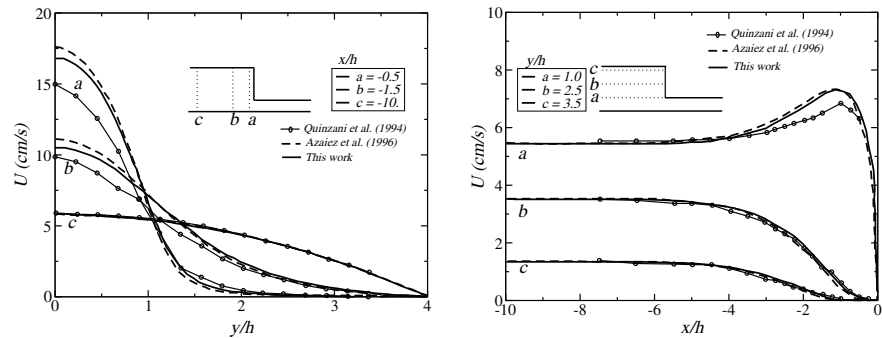


Fig. 11. Velocity profiles on vertical (left) and horizontal (right) lines in the upstream section using the single-mode Giesekus model.

rate on the performance of the interpolation schemes is higher than that of the shear rate.

For a quantitative comparison between the *upwind* scheme and other three schemes, the percentage normalized error (PNE) and the average percentage normalized error (APNE) were calculated. PNE was calculated according to Eq. (14), using the predictions of the *upwind* scheme as X_j^i and the correspondent predictions with *Gamma 1* scheme as X_j^{ref} . The average percentage normalized error was defined as:

$$\text{APNE} = \frac{\sum_{j=1}^N (|X_j^i - X_j^{\text{ref}}| / \max(|X_j^{\text{ref}}|))}{N} \times 100 \quad (15)$$

where N is the number of points on the line considered. Since for all variables the higher differences among the two schemes were observed when comparing the profiles on line “a” of Fig. 8, the normalized error was calculated using only data of these profiles. The comparison between *upwind* and *Gamma 1* schemes, shown in Table 6, shows that despite of obtaining values of PNE close to 7% for the first normal stress difference, the values of APNE are acceptable, less than 1.2%. Taking into account that large deviations occur only in a specific region of the flow, the accuracy of the *upwind* scheme was considered satisfactory and this scheme was selected to be used in the remaining tests.

Table 6

Percentage and percentage averaged normalized errors of the *upwind* scheme compared with the *Gamma 1* scheme for the line “a” of Fig. 8.

Scheme	PNE		APNE	
	τ_{xy}	N_1	τ_{xy}	N_1
<i>Upwind</i>	4.441	6.922	0.741	1.143

3.1.3. Simulations with high Deborah numbers and deformation rates

Fig. 10 shows how the De values affect the velocity and the first normal stress difference at the centerline using single-mode Giesekus model with the parameters listed in Table 3. The flow along the centerline has an elongational nature, and the elongational properties of the rheological model play an important role in determining the way it responds to the accelerating forces when it approaches the corner [28]. Giesekus model predicts an overshoot of the velocity for all values of the *Deborah* number near to the re-entrant corner. The overshoot is higher as higher is the De values. The first normal stress difference has its values increased with the increase of De number. At high De number it is found that the symmetry around the zero point is lost.

The results show the stability of the implemented methodology to simulate flows at higher deformation rates. The results for $De=50.0$ were obtained with a deformation rate of $1666.67 [\text{s}^{-1}]$.

3.1.4. Comparison between simulation and experimental data

In this section, the results obtained with the parameters described in the previous section using Giesekus model are presented. In order to verify the predictions of *viscoelasticFluidFoam* solver, these results are compared with the numerical solution obtained by Azaiez et al. [28] and with the experimental data presented by Quinzani et al. [26].

Figs. 11–13 presents the profiles of velocity, shear stress and first normal stress difference, respectively, on vertical and horizontal lines located in the upstream section. In all cases good agreement with the numerical results of Azaiez et al. [28] was observed, especially in the developed flow region. The small differences observed can be attributed to the fact that numerical scheme and meshes used by Azaiez et al. [28] were not the same as those used in the present work. With relation to the experimental data, both numerical solutions presented good qualitative agreement, with

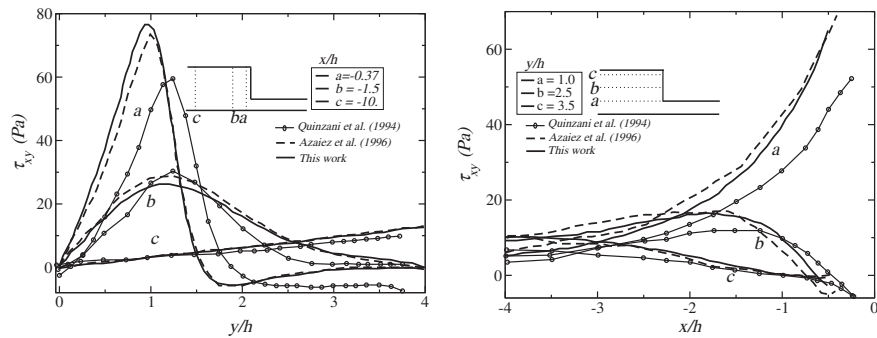


Fig. 12. Shear stress profiles on vertical (left) and horizontal (right) lines in the upstream section using the single-mode Giesekus model.

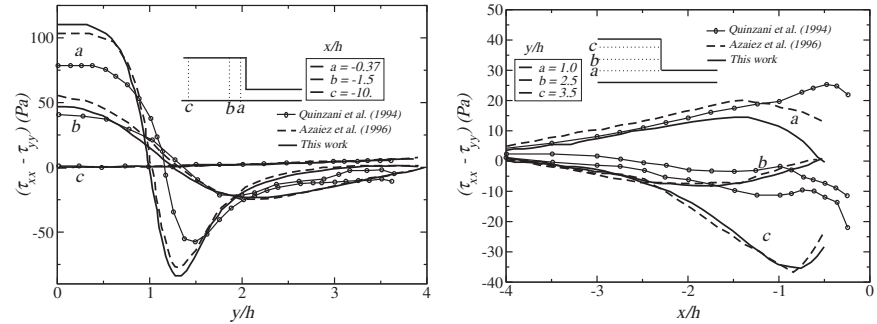


Fig. 13. First normal stress difference profiles on vertical lines in the upstream section (left) and on horizontal lines crossing the flow domain (right) using the single-mode Giesekus model.

the highest deviations occurring near the contraction. The only exception to this was the profile of first normal stress difference on the horizontal line “c” (Fig. 13, right), for which both numerical solutions show a continuous increase near the contraction, differently from what is observed in the experimental data. The differences among numerical and experimental data may be partially explained by the use of a single relaxation mode, which makes it difficult to completely characterize the stress field, mainly in high elongation rate regions.

Similar comparison at the downstream section (Figs. 14–16) shows that the same general tendencies discussed above for the upstream section are observed downstream, but with the differences among numerical and experimental results becoming more intense. This is in agreement with the aspects discussed in the previous paragraph and with the higher deformation rates occurring in the downstream section.

3.2. Testing of the implementation of the multimode approach for polymeric stress

The testing of the implementation of the multimode approach was conducted with the same test problem as in Section 3.1, using a 4-mode Giesekus model. The values of the parameters of this model were determined by Azaiez et al. [36] and are shown in Table 7. The predictions of the viscoelasticFluidFoam solver for the flow conditions of Run 3 of Quinzani et al. [26] ($Re = 0.27$) are shown in Fig. 17 together with the corresponding experimental data of Quinzani et al. [26] and numerical results of Azaiez et al. [36]. It can be observed that the numerical results obtained in this work presented good agreement with numerical results of Ref. [36], indicating that the multimode approach was also adequately implemented. The small differences found can again be attributed to the different meshes and numerical schemes used in Ref. [36].

The fact that the use of a multimode version of the constitutive model improves significantly the fitting of the model to the experimental data, as can be observed by comparing Fig. 17 (left) with Fig. 16 (left), indicates the importance of an efficient implementation of the multimode approach. In this sense, it is important to mention that the computational time of simulations with the 4-mode Giesekus were only about twice those of the simulation with the single-mode Giesekus. This can be explained because most of the computational cost is associated with the resolution of the momentum equation and the pressure correction step (PISO).

Table 7
Parameters of 4-mode Giesekus model estimated by Azaiez et al. [36] for the polyisobutylene solution of Ref. [26].

Mode	α	λ [s]	η_p [Pa s]	η_s [Pa s]	De
1	0.5	0.6855	0.0400	0.002	15.94
2	0.2	0.1396	0.2324	0.002	3.25
3	0.3	0.0389	0.5664	0.002	0.90
4	0.2	0.0059	0.5850	0.002	0.14

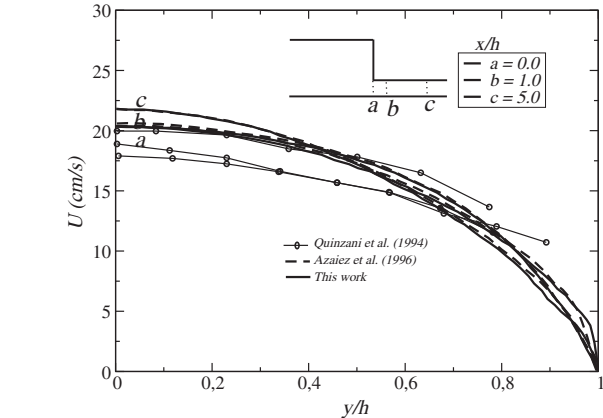


Fig. 14. Velocity profiles on vertical lines in the downstream section using the single-mode Giesekus model.

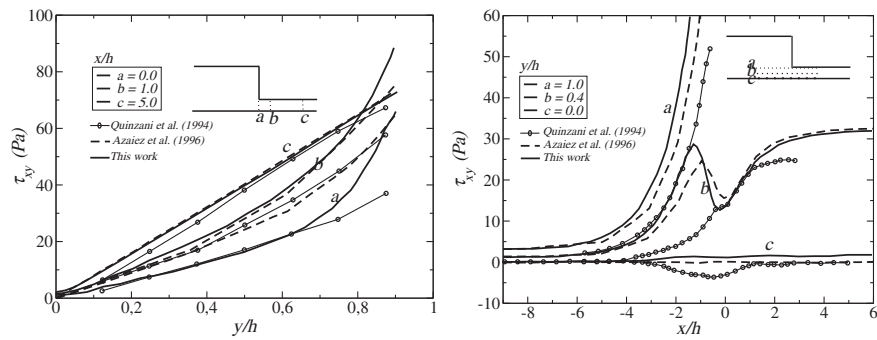


Fig. 15. Shear stress profiles on vertical lines in the downstream section (left) and on horizontal lines crossing the flow domain (right) using the single-mode Giesekus model.

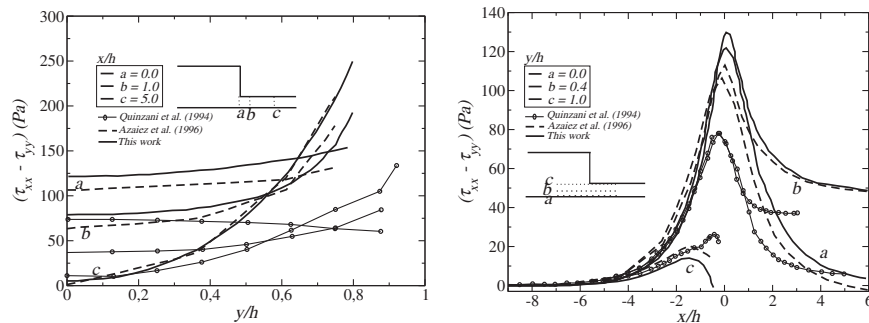


Fig. 16. First normal stress difference profiles on vertical lines in the downstream section (left) and on horizontal lines crossing the flow domain (right) using the single-mode Giesekus model.

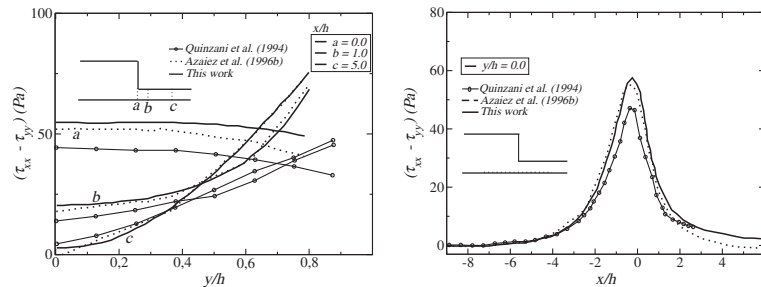


Fig. 17. First normal stress difference profiles on vertical (left) and horizontal (right) lines in the downstream section using the 4-mode Giesekus model.

At this point it is worthy to mention that Mitsoulis [27] simulated the experiments of Quinzani et al. [26] using a multimode K-BKZ integral mode, achieving better agreement with experiments than that found with the 4-mode Giesekus mode. However, a comparison with the results of integral models is beyond the goals of this work.

3.3. Evaluation of the LPTT and FENE-P models

Fig. 18 shows the predictions of LPTT and FENE-P for the first normal stress difference. For comparison, predictions with the Giesekus model are also presented in Fig. 18. Differences of prediction among the three models can be observed, with FENE-P

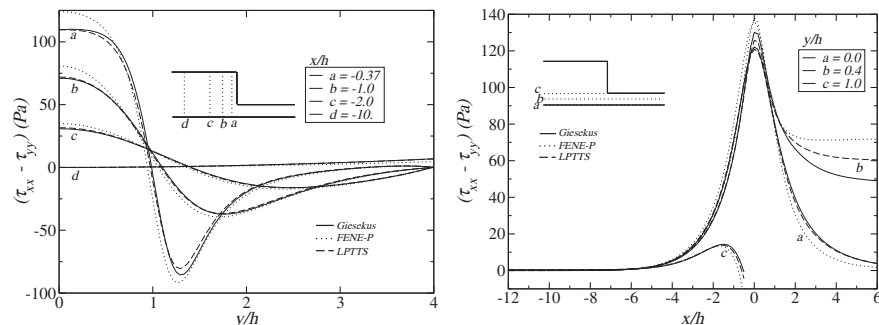


Fig. 18. First normal stress difference profiles predicted with FENE-P and LPTT models on downstream section (left) and on horizontal lines crossing the flow domain (right).

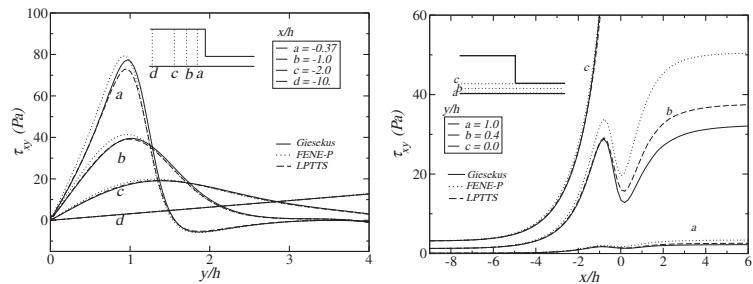


Fig. 19. Shear stress profiles predicted with FENE-P and LPTT models on upstream section (left) and on horizontal lines crossing the flow domain (right).

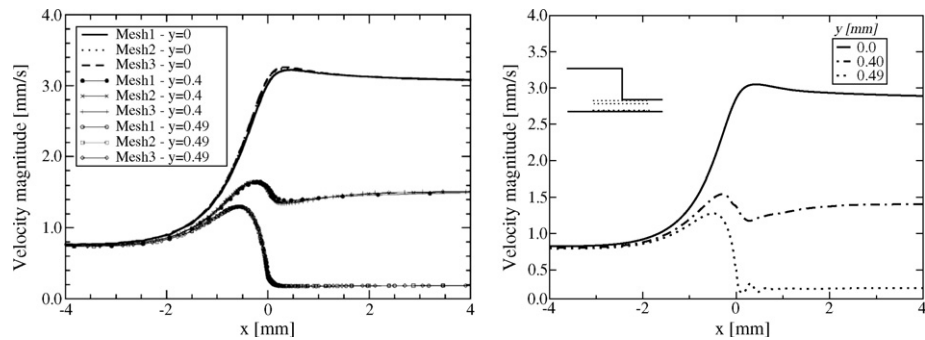


Fig. 20. Results of velocity magnitude along centerline ($y=0$), $y=0.4$ and along $y=0.49$ using the 4-mode DCP model. Literature data [37] (left) and results obtained in this work (right).

presenting the higher deviations with relation to the Giesekus model – as it can be seen especially in curve “b” of Fig. 18 (right) – and also to experimental data (Fig. 16). Similar trends in terms of differences among the three models are also observed for the predictions of shear stress, as shown in Fig. 18. Additionally, it must be mentioned that these results are in good agreement with those presented by Azaiez et al. [28] and, consequently, that these differences among the predictions of the three models are related exclusively to the intrinsic differences among them.

3.4. Evaluation of the DCP multimode

DCP model implementation was tested by comparison with data of Clemeur et al. [37] for a planar abrupt contraction similar to that shown in Fig. 1, but with $2H=4.10\text{ mm}$ and $h=1\text{ mm}$, giving a contraction ratio of 4.1:1. In both upstream and downstream channel a length of 80 mm was used, with a mesh similar to Mesh 2 of Section 3.1.1 and with a number of cells of 22500. As in Clemeur et al. [37], an apparent downstream wall shear rate of 12.4 s^{-1} was used, giving a Weissenberg number of 50.0. The corresponding values for the parameters of DCP model are listed in Table 8 and

Table 8 Parameters of 4-mode DCP model [37].					
Mode	λ_{0b} [s]	λ_{0s} [s]	η_p [Pa s]	ξ	q
1	0.02	0.01	1.03×10^3	0.2	1.0
2	0.2	0.1	2.22×10^3	0.2	1.0
3	2.0	1.0	4.16×10^3	0.07	6.0
4	20.0	20.0	1.322×10^3	0.05	18.0

the definition of the index PSD (*Principal Stress Difference*), used as parameter of comparison, is given in Eq. (16).

$$PSD = \sqrt{(\tau_{yy} - \tau_{xx})^2 + 4\tau_{xy}^2}$$
 (16)

Predictions for velocity magnitude and principal stress difference are presented in Figs. 20 and 21, respectively. The good agreement with the results of Clemeur et al. [37] indicates that the model was correctly implemented and the used methodology performed adequately also for this model.

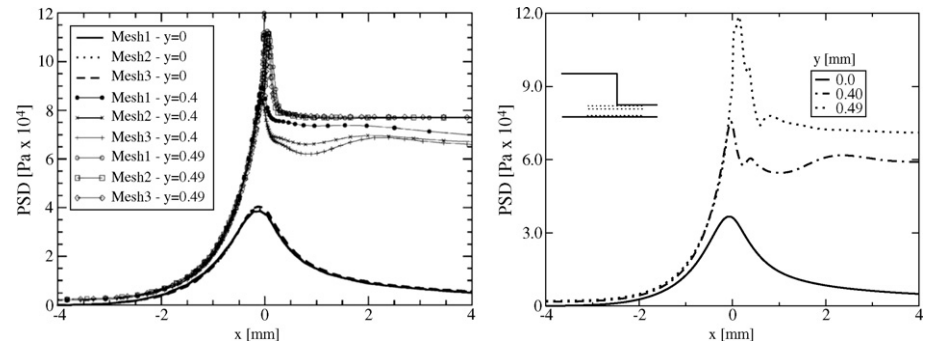


Fig. 21. Results of PSD along centerline ($y=0$), $y=0.4$ and along $y=0.49$ using the 4-mode DCP model. Literature data [37] (left) and results obtained in this work (right).

4. Conclusion

This work presented a new numerical methodology based on the split-stress tensor approach and the concept of equilibrium stress tensor to treat high Weissenberg number problems using any differential constitutive equations and a new tool for CFD simulation of viscoelastic fluids, the viscoelasticFluidFoam solver. Extensive testing has shown that a viscoelastic flow solver assembled in this manner works in a stable and efficient manner. Mesh convergence analysis and comparison of the predictions of the viscoelasticFluidFoam solver with the numeric results of Azaiez et al. [36] and the experimental data obtained by Quinzani et al. [26] showed the consistency of the developed tool. Several different constitutive models was tested and the results are in agreement with literature data, confirming that the adopted methodology was successful.

The choice of the software OpenFOAM as platform for the development of this solver has proved to be an adequate choice. It has allowed a clear straightforward and numerically stable implementation of a set of complex differential constitutive equations, both in single and multimode relaxation forms, and the use of several available numerical schemes which dealt adequately with the inherent difficulties of the analysis of viscoelastic flows. With the availability of a reasonable set of viscoelastic constitutive models and the intrinsic characteristics of the OpenFOAM tool, the viscoelasticFluidFoam solver provides a great potential for analysis of viscoelastic flows and further developments focused on modeling and simulation of food and polymer processing operations.

Acknowledgements

The authors would like to thank CAPES and CNPq for the financial support.

Appendix A.

The implementation of the different equations involved (continuity, momentum, and a constitutive equation) was done using the OpenFOAM C++ resources which make possible the definition of variables directly as vectors or tensors. This avoids the need of breaking the equations in all its components, through the use of a symbolic representation which is quite similar to the mathematical language. In this way, for example, the symbolic representation of Eq. (2) in OpenFOAM language is:

```
fVVectorMatrix UEqn
(
    fvm::ddt(rho, U) + fvm::div(phi, U) - fvc::div(tau)
);
solve( UEqn == - fvc::grad(p) );
```

where $\phi = S_f \cdot (\rho \mathbf{u})_f$ and S_f is the cell face surface, *fvm* (*finite volume method*) is a class used for implicit operations and *fvc* (*finite volume calculus*) is a class used for explicit operations. The terms of the equation for velocity (\mathbf{u}) are stored in a matrix that contains the equations for the three components of the vector \mathbf{u} (*fVVectorMatrix*) named *UEqn* and this equation is solved with the command `solve(UEqn == - fvc::grad(p))` in which the pressure gradient is included to complete the equation. The inclusion of the pressure gradient only in this last command and not in the definition of the *UEqn* matrix is due to the use of the SIMPLE or PISO algorithm.

Regarding the implementation of the constitutive equations for polymeric stress tensor, the description was done using the imple-

mentation of Giesekus model as example, rearranged as:

$$\frac{1}{\lambda_K} \tau_{PK} + \overset{\nabla}{\tau}_{PK} + \frac{\alpha_K}{\eta_{PK}} (\tau_{PK} \cdot \tau_{PK}) = 2 \frac{\eta_{PK}}{\lambda_K} \mathbf{D} \quad (17)$$

which in the symbolic representation of OpenFOAM is given by:

```
solve
(
    fvm::ddt(tauP) + fvm::div(phi, tauP)
    ==
    etaP / lambda * twoSymm( L ) + twoSymm( C )
    - (alpha / etaP) * (tauP & tauP) - fvm::Sp(1/lambda, tauP)
);
```

where the operator $\&$ defines the inner product between two variables, the function `twoSymm()` calculates the sum between the argument and its transpose, i.e., for a generic tensor \mathbf{A} , `twoSymm(A) = $\mathbf{A} + \mathbf{A}^T$` . The variable \mathbf{L} is the velocity gradient ($\mathbf{L} = \text{fvc}::\text{grad}(\mathbf{U})$), and \mathbf{C} is defined as: $\mathbf{C} = (\tau_{PK} \cdot \nabla \mathbf{u})^T$. So the term `twoSymm(C)` corresponds to the sum of inner products in the definition of the upper convected derivative:

$$\text{twoSymm}(\mathbf{C}) = (\tau_{PK} \cdot \mathbf{L}) + (\tau_{PK} \cdot \mathbf{L})^T = [\tau_{PK} \cdot \nabla \mathbf{u}] + [\tau_{PK} \cdot \nabla \mathbf{u}]^T.$$

As the equation for the stress tensor assumes the form of a symmetric tensor, the class *fVSymmTensorMatrix* was used to store the terms of this equation for stress to take advantage of the fact that only six components are required to describe a symmetric tensor. The operation `solve()` is used to solve the stress equation. After solving the equation for each mode, the extra elastic stress tensor is obtained summing all contributions of the individual modes using Eq. (6).

References

- [1] R.B. Bird, R.C. Armstrong, O. Hassager, Dynamics of Polymeric Liquids, vol. 1, Fluid Mechanics, John Wiley, New York, 1987.
- [2] C. Macosko, Rheology: Principles, Measurements and Applications, VCH Publishers, 1994.
- [3] M.A. Alves, P.J. Oliveira, F.T. Pinho, A convergent and universally bounded interpolation scheme for the treatment of advection, *Int. J. Numer. Meth. Fluids* 41 (2003) 47–75.
- [4] A.R. Muniz, A.R. Secchi, N.S.M. Cardozo, High-order finite volume method for solving viscoelastic fluid flows, *Braz. J. Chem. Eng.* 25 (2008) 53–58.
- [5] M.G.N. Perera, K. Walters, Long-range memory effects in flows involving abrupt changes in geometry, *J. Non-Newtonian Fluid Mech.* (1977) 49–81.
- [6] D. Rajagopalan, R.C. Armstrong, R.A. Brown, Finite element methods for calculation of steady, viscoelastic flow using constitutive equations with Newtonian viscosity, *J. Non-Newtonian Fluid Mech.* 36 (1990) 159–192.
- [7] R. Guénette, M. Fortin, A new mixed finite element method for computing viscoelastic flows, *J. Non-Newtonian Fluid Mech.* 60 (1995) 27–52.
- [8] J. Sun, N. Phan-Thien, R.I. Tanner, An adaptive viscoelastic stress splitting scheme and its applications: AVSS/SI and AVSS/SUPG, *J. Non-Newtonian Fluid Mech.* 65 (1996) 75–91.
- [9] H.G. Weller, G. Tabor, H. Jasak, Fureby, A tensorial approach to computational continuum mechanics using object orientated techniques, *Comput. Phys.* 12 (1998) 620–631.
- [10] H. Jasak, Error Analysis and Estimation for the Finite Volume Method with Applications to Fluid Flows, PhD Thesis, Imperial College, University of London, 1996.
- [11] S.-C. Xue, R.I. Tanner, N. Phan-Thien, Numerical modelling of transient viscoelastic flows, *J. Non-Newtonian Fluid Mech.* 123 (2004) 33–58.
- [12] J.G. Oldroyd, On the formulation of rheological equations of state, *Proc. R. Soc. A200* (1950) 523–541.
- [13] H. Giesekus, A simple constitutive equation for polymer fluids based on the concept of deformation-dependent tensorial mobility, *J. Non-Newtonian Fluid Mech.* 11 (1982) 69–109.
- [14] J.L. White, A.B. Metzner, Development of constitutive equations for polymeric melts and solutions, *J. Appl. Polym. Sci.* 7 (1963) 1867–1889.
- [15] A.I. Leonov, Non-equilibrium thermodynamics and rheology of viscoelastic polymer media, *Rheol. Acta* 15 (1976) 85–98.
- [16] R.G. Larson, Constitutive Equations for Polymer Melts and Solutions, Butterworths, Boston, 1988.
- [17] R.B. Bird, P.J. Dotson, N.L. Johnson, Polymer solution rheology based on a finitely extensible bead-spring chain model, *J. Non-Newtonian Fluid Mech.* 7 (1980) 213–235.
- [18] M.D. Chilcott, J.M. Rallison, Creeping flow of dilute polymer solutions past cylinders and spheres, *J. Non-Newtonian Fluid Mech.* 29 (1988) 381–

- 432.
- [19] N. Phan-Thien, R.I. Tanner, A new constitutive equation derived from network theory, *J. Non-Newtonian Fluid Mech.* 2 (1977) 353–365.
 - [20] T.C.B. McLeish, R.G. Larson, Molecular constitutive equations for a class of branched polymers: the pom–pom polymer, *J. Rheol.* 42 (1998) 81–110.
 - [21] W.M.H. Verbeeten, G.W.M. Peters, F.P.T. Baaijens, Differential constitutive equations for polymer melts: the extended Pom–Pom model, *J. Rheol.* 45 (2001) 823–844.
 - [22] N. Clemeur, R.P.G. Rutgers, B. Debbaut, On the evaluation of some differential formulations for the pom–pom constitutive model, *Rheol. Acta* 42 (2003) 217–231.
 - [23] J.H. Ferziger, M. Perić, *Computational Methods for Fluid Dynamics*, Springer Verlag, Berlin/New York, 1995.
 - [24] S.V. Patankar, D.B. Spalding, A calculation procedure for heat, mass and momentum transfer in three-dimensional Parabolic flows, *Int. Heat Mass Transf.* 115 (1972) 1787–1803.
 - [25] R.I. Issa, Solution of the implicitly discretized fluid flow equations by operator-splitting, *J. Comput. Phys.* 62 (1986) 40–65.
 - [26] L.M. Quinzani, R.C. Armstrong, R.A. Brown, *J. Non-Newtonian Fluid Mech.* 52 (1994) 1–36.
 - [27] E. Mitsoulis, Numerical simulation of planar entry flow for a polyisobutylene solution using an integral constitutive equation, *J. Rheol.* (1993) 1029–1040.
 - [28] J. Azaiez, R. Guénette, A. Ait-Kadi, Numerical simulation of viscoelastic flows through a planar contraction, *J. Non-Newtonian Fluid Mech.* 62 (1996) 253–277.
 - [29] J. Lee, J. Zhang, C.-C. Lu, Incomplete LU preconditioning for large scale dense complex linear systems from electromagnetic wave scattering problems, *J. Non-Newtonian Fluid Mech.* 185 (2003) 158–175.
 - [30] D.A.H. Jacobs, Preconditioned conjugate gradient methods for solving systems of algebraic equations, Technical Report RD/L/N193/80, Central Electricity Research Laboratories, 1980.
 - [31] M.A. Ajiz, A. Jennings, A robust incomplete cholesky-conjugate gradient algorithm, *J. Numer. Meth. Eng.* (1984) 949–966.
 - [32] E. Ryssel, P.O. Brunn, Comparison of a quasi-Newtonian fluid with a viscoelastic fluid in planar contraction flow, *J. Non-Newtonian Fluid Mech.* 86 (1999) 309–335.
 - [33] H. Jasak, H. Weller, A. Gosman, High resolution NVD differencing scheme for arbitrarily unstructured meshes, *Int. J. Numer. Meth. Fluids* 31 (1999) 431–449.
 - [34] A. Harten, High-resolution schemes for hyperbolic conservation laws, *J. Comput. Phys.* 49 (1983) 357–393.
 - [35] STAR-CD, *Star-CD Methodology Manual*, Computational Dynamics Ltd., UK, 2002.
 - [36] J. Azaiez, R. Guénette, A. Ait-Kadi, Entry flow calculations using multi-mode models, *J. Non-Newtonian Fluid Mech.* 66 (1996) 271–281.
 - [37] N. Clemeur, R.P.G. Rutgers, B. Debbaut, Numerical simulation of abrupt contraction flows using the double convected Pom–Pom model, *J. Non-Newtonian Fluid Mech.* 117 (2004) 193–209.